Journal of Power Sources 535 (2022) 231471

Contents lists available at ScienceDirect

Journal of Power Sources

journal homepage: www.elsevier.com/locate/jpowsour

Nitrogen–doped graphitic mesoporous carbon materials as effective sulfur imbibition hosts for magnesium-sulfur batteries

Minseok Lee [a,b,1], Minji Jeong [a,1], Youn Shin Nam [c], Janghyuk Moon [c], Minah Lee [a], Hee-Dae Lim [a], Dongjin Byun [b], Taeeun Yim [d], Si Hyoung Oh [a,e,*]

[a] Energy Storage Research Center, Korea Institute of Science and Technology, 5, Hwarang-ro 14-gil, Seongbuk-gu, Seoul, 02792, Republic of Korea
[b] Department of Materials Science and Engineering, Korea University, 145, Anam-ro, Seongbuk-gu, Seoul, 02841, Republic of Korea
[c] School of Energy Systems Engineering, Chung-Ang University, Heukseok-Ro, Dongjak-Gu, Seoul, 06974, Republic of Korea
[d] Department of Chemistry, Incheon National University, 119, Academy-ro, Yeongsu-gu, Incheon, 22012, Republic of Korea
[e] Division of Energy & Environment Technology, Korea University of Science and Technology, 5, Hwarang-ro 14-gil, Seongbuk-gu, Seoul, 02792, Republic of Korea

HIGHLIGHTS

- N-doped graphitic mesoporous carbon is utilized as a host for S_8 imbibition.
- Suitable surface moiety and wall structure of carbon host is proposed.
- The pyridinic-N stronly binds MgPS and accelerates its dissociation.
- Synergic effect enables an enhanced performance for Mg–S batteries.

GRAPHICAL ABSTRACT

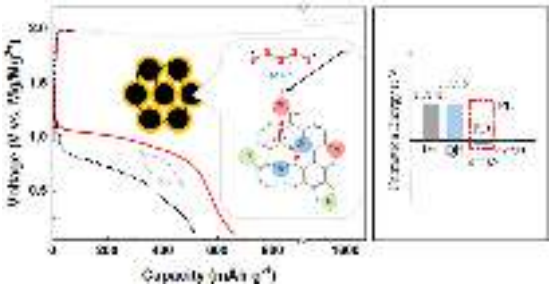

ARTICLE INFO

Keywords:
Nitrogen-doped mesoporous carbon
Polysulfide fragmentation
Catalyst
Magnesium-sulfur battery
Density functional theory
Pyridinic nitrogen

ABSTRACT

The true potential of Mg–S batteries is not yet realized despite its great advantages in material cost and safety. This is due to the lethargic reaction kinetics involved in the dissociation of Mg polysulfide (MgPS) on the cathode. Herein, we propose nitrogen–doped mesoporous carbon (N*d*MC) materials with suitable nitrogen content and surface moieties that can be utilized as catalytic hosts to enhance polysulfide fragmentation and electron access to the redox active sites in Mg–S batteries. In controlled N*d*MC, the surface nitrogen atoms located at the pyridinic positions can strongly bind MgPS and accelerate the reduction of MgPS to MgS, while the graphitic wall structure facilitates facile electron transport to the reaction sites. This synergic effect enables the composite electrode made of tuned N*d*MC and sulfur to exhibit an enhanced reversible capacity and good cycling capacity retention in Mg–S batteries. This study offers a new strategy for improving the performance of Mg–S batteries by fine-tuning the structural properties of the carbon hosts.

* Corresponding author. Energy Storage Research Center, Korea Institute of Science and Technology, 5, Hwarang-ro 14-gil, Seongbuk-gu, Seoul, 02792, Republic of Korea.
E-mail address: sho74@kist.re.kr (S.H. Oh).
[1] These authors contributed equally to this work.

https://doi.org/10.1016/j.jpowsour.2022.231471
Received 21 February 2022; Received in revised form 1 April 2022; Accepted 12 April 2022
Available online 21 April 2022

1. Introduction

The recent remarkable growth of electric vehicles (EVs) and energy storage systems (ESSs), necessitates the development of new rechargeable batteries that are superior to conventional Li-ion batteries (LIBs) in terms of cost-competitiveness and safety. Owing to their environmentally benign and air-stable composition, the combination of Mg and S as electrode materials can offer an ideal chemistry to meet the stringent requirements for rechargeable batteries. Specifically, these elements are not only abundant in the earth's crust (2.33%), but they can also provide a competitive energy density of 3,200 Wh L^{-1} (or 1,600 Wh kg^{-1} based on the total mass of active materials) from their conversion-type electrode reactions, which would enable a substantial extension in the driving range of EVs [1–3].

Despite these obvious advantages, the prospect of Mg–S batteries has been plagued by the technical challenges involved in the development of functional electrolytes that are compatible with both sulfur and Mg metal electrodes. Furthermore, the lack of a comprehensive understanding of the reaction mechanisms have been hindering the enhancement of reaction kinetics and the cycling stability associated with sulfur cathodes. Intensive research spanning over a decade has led to significant progress in the development of functional electrolytes, and several promising electrolyte candidates have been proposed, which exhibit both efficient Mg plating stripping as well as good chemical stability towards sulfur. A few such examples would be ethereal solutions of Hauser bases (magnesium amide bases) combined with aluminum chloride ($AlCl_3$) [4–6], boron-centered magnesium electrolyte series (BCM) based on the combination of tris (2H-hexafluoroisopropyl)borate (THFPB) with magnesium halides [7–9], and ethereal solutions of magnesium bis(trifluorosulfonyl)imide ($MgTFSI_2$) with $MgCl_2$ [10–12], etc. However, the lethargic conversion kinetics on the sulfur cathode still remains a major roadblock [1–3]. In Mg–S batteries so far, ether-based solvents have been frequently employed in order to secure reversible Mg plating-stripping on the anode. While the exact reaction mechanism of the sulfur cathode remains obscure and is likely dependent on the particular electrolyte systems employed, the sparse solubility and instability of the reaction intermediate Mg polysulfide (MgPS, MgS_n, $3 \leq n \leq 8$), in ethereal solvents is often speculated to be one of the main causes for the slow reaction kinetics [13–15]. Bieker et al. showed that the solubility of MgPS in most ethereal solvents was much lower than that of Li polysulfides (LiPS), by analyzing the UV–Vis spectra of the solutions [13,14]. They observed that MgPS was hardly soluble in dimethoxyethane (DME), one of the common solvents used in Mg batteries. They also proposed that the use of solvents with much higher relative dielectric permittivity (ε_r) and/or higher Gutmann donor number (DN), such as dimethylformamide (DMF, $\varepsilon_r = 36.1$, DN = 26.6) and dimethyl sulfoxide (DMSO, $\varepsilon = 45.0$, DN = 29.8), could enhance the solubility of MgPS, which might induce faster solution-phase reaction routes. However, the poor chemical stability of these solvents upon intimate contact with Mg metal limits their practical use. Moreover, the low but finite solubility of the intermediate MgPS species in these solvents could cause the 'polysulfide shuttle' and gradual degradation of the Mg anode [5,12].

Meanwhile in conventional Li–S battery research, the key conundrums to be resolved in order to overcome the slow reaction kinetics are, reportedly, identifying the actual redox-active polysulfide species and enhancing the disproportionation of LiPS in the given electrolyte system [16–18]. Catalysts that enable the fast dissociation of polysulfide chains have been intensively studied in Li–S batteries and a few reported examples include transition metal oxides [19], sulfides [20], nitrides [21], carbides [22] as well as various functionalized carbon materials [23–25]. These materials enhance the dissociation of LiPS by deploying them on sulfur cathodes or separators, to form an appropriate adhesive bonding on their surfaces and hence destabilizing intramolecular bonding in the polysulfide [26,27]. A similar strategy may be applied to boost the reaction kinetics of Mg–S as well, which suffers from slower kinetics than Li–S [1–3].

In this study, we demonstrate that nitrogen-doped mesoporous carbon materials (N*d*MC) could be utilized as promising catalytic hosts for enhancing MgPS fragmentation in BCM electrolytes, which exhibit substantial MgPS solubility. This was enabled by the synergetic effect of the portfolios of nitrogen moieties in the N*d*MC structure, which not only retained the strong chemical affinity to MgPS but also provided a favorable electronic structure to promote facile electron access to the redox sites. This led to enhanced electrochemical activity in Mg–S batteries, specifically, reversible capacity and capacity retention. This study offers a new strategy for improving the performance of future Mg–S batteries by fine-tuning the structural properties of the carbon hosts.

2. Experimental section

2.1. Preparation of NdMC

N-doped mesoporous carbon (N*d*MC) was synthesized with SBA-15 (Silica, Sigma Aldrich) and Fe-phthalocyannine (Fe-Pc, Sigma Aldrich) using a previously reported method [28,29]. First, SBA-15 [30] and Fe-Pc were gently ground using a mortar and pestle in a 1:1 wt ratio. The mixture was then pressed into a pellet, and subjected to heat treatment for 3 h at 750 °C or 900 °C under an argon atmosphere to obtain the SBA-15/carbon composite. The SBA-15 template was then leached in a 10 wt% HF solution. The filtered product was thoroughly washed and dried overnight in an oven at 80 °C.

2.2. Preparation of S_8@NdMC composite cathode

S_8@N*d*MC composite was prepared using a melt-diffusion strategy, in which S_8 (Alfa Aesar, 99.5%) and N*d*MC powders were mixed in a 1:1 wt ratio, pressed into a pellet, and put into the autoclave. They were subsequently stored in an oven at 140 °C for 3 h. For cathode construction, a homogeneous slurry containing the S_8@N*d*MC composite, super P conductor, and polyvinylidene fluoride (PVdF) solution in N-methyl-2-pyrrolidinone (NMP) (70:5:25 wt%) was prepared with a ball-mixer apparatus (Pulverisette 23, Fritsch), cast onto carbon-coated aluminum foil current collector, and completely dried in an oven at 50 °C overnight. The typical loading of the active material was 0.70 (±0.10) mg cm^{-2}.

2.3. Preparation of electrolytes

Boron-centered anion-based magnesium (BCM) electrolyte was prepared using a known method [7–9]. THFPB (TCl, 1.024 g) was first dissolved in dimethoxyethane (DME, 2 mL) in a glass vial, to which ground MgF_2 (Sigma Aldrich, 0.0062 g) was added and dissolved. Subsequently, the resulting solution was stirred overnight. All preparations were handled in an argon-filled glove box with oxygen and moisture levels strictly maintained below 0.1 ppm.

2.4. Manufacturing of the Mg–S cell using NdMC

The electrochemical properties were investigated using 2032-type coin cells prepared by assembling the S_8@N*d*MC composite cathode, a magnesium metal anode, a polyethylene separator (SK-innovation, 20 μm), and the BCM electrolyte in an argon-filled glove box. The amount of electrolyte used in each coin cell was 80 μL. Galvanostatic measurements were carried out using a battery system (Series4000, MACCOR, USA), by varying the potential from 0.1 to 2.5 V at different current densities (from 0.02 C to 0.1 C, 1 C = 1,675 mAh g^{-1}). The specific capacity was calculated based on the mass of sulfur. Cyclic voltammetry (CV) measurements were performed using VMP3 potentiostat, Biologic Science Instruments over the range 0.3–2.5 V (vs. Mg/Mg^{2+}) at a scan rate of 0.02 mV s^{-1}.

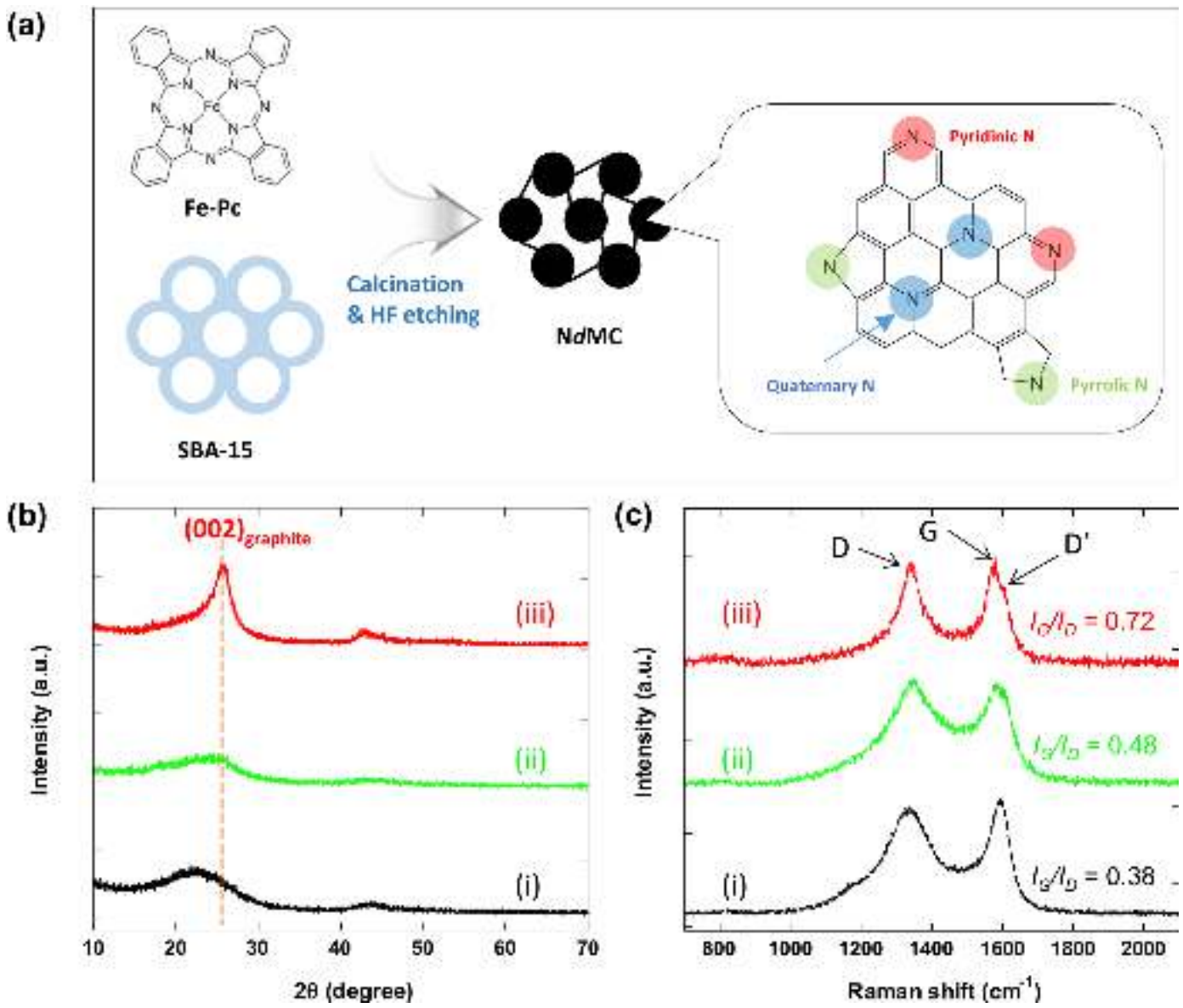

Fig. 1. (a) Schematic of the synthesis of N*d*MC materials with various N-doping moieties, (b) XRD patterns and (c) Raman spectra for (i) CMK-3, (ii) N*d*MC-750, and (iii) N*d*MC-900.

2.5. Preparation of magnesium polysulfide, Mg(1-methylimidzole)$_6$]S_8

Mg(1-methylimidzole)$_6$]S_8 was obtained using a previously reported method [31]. Briefly, Mg metal powder (0.167 g) and sulfur powder (1.801 g) was stirred in 1-methylimidazole (30 mL) at 95 °C for 12 h. The resulting red solution was filtered to remove undissolved species. The solution was further treated with toluene, to form red crystalline precipitates.

2.6. Measurement and characterization

The morphology of the materials was observed by field-emission scanning electron microscopy (FE-SEM, Inspect F, FEI Corp.) at an accelerating voltage of 15 kV with an Energy Dispersive Spectroscopy (EDS) attachment for chemical analysis. X-ray diffraction (XRD) patterns were obtained using Cu-Kα radiation (λ = 1.54 Å) at 40 kV and 200 mA (Dmax2500, Rigaku Corp.). The surface area and pore size distribution of N*d*MC were estimated by Brunauer-Emmett-Teller (BET) analysis using the adsorption branch of the N_2 isotherm at 77 K (ASAP2010, Micromeritics, USA). Raman spectra were measured using a 532 nm laser excitation (InVia Raman Microscope, Renishaw, UK). The surface structural characteristics of the N*d*MC were examined using X-ray photoelectron spectroscopy (XPS, Nexsa, Thermo Fisher Scientific, UK) obtained using monochromatic Al-Kα radiation ($h\nu$ = 1486.6 eV) in a 6.7×10^{-8} Pa, and the data were calibrated by setting the binding energy of C 1s to 284.6 eV. Thermogravimetric analysis (TGA) for S_8@N*d*MC composites was carried out in flowing N_2 atmosphere with a heating rate of 20 °C min^{-1} up to 600 °C (SDT Q600, TA Instruments). The amount of dissolved species in the solution was measured using an inductively coupled plasma-optical emission spectrometer (ICP-OES, Optima 5300 DV, PerkinElmer, USA). UV–Vis spectra were measured using a DH-2000 (Ocean Optics) in the range of 250–800 nm.

2.7. Density functional theory calculation

Mg adsorption energies were computed using Projector-augmented wave (PAW) pseudopotentials in the density functional theory (DFT) calculation framework, as implemented in the Vienna *ab initio* simulation package (VASP) [32,33]. The Perdew-Burke-Ernzerhof (PBE) implementation of the generalized gradient approximation (GGA) was

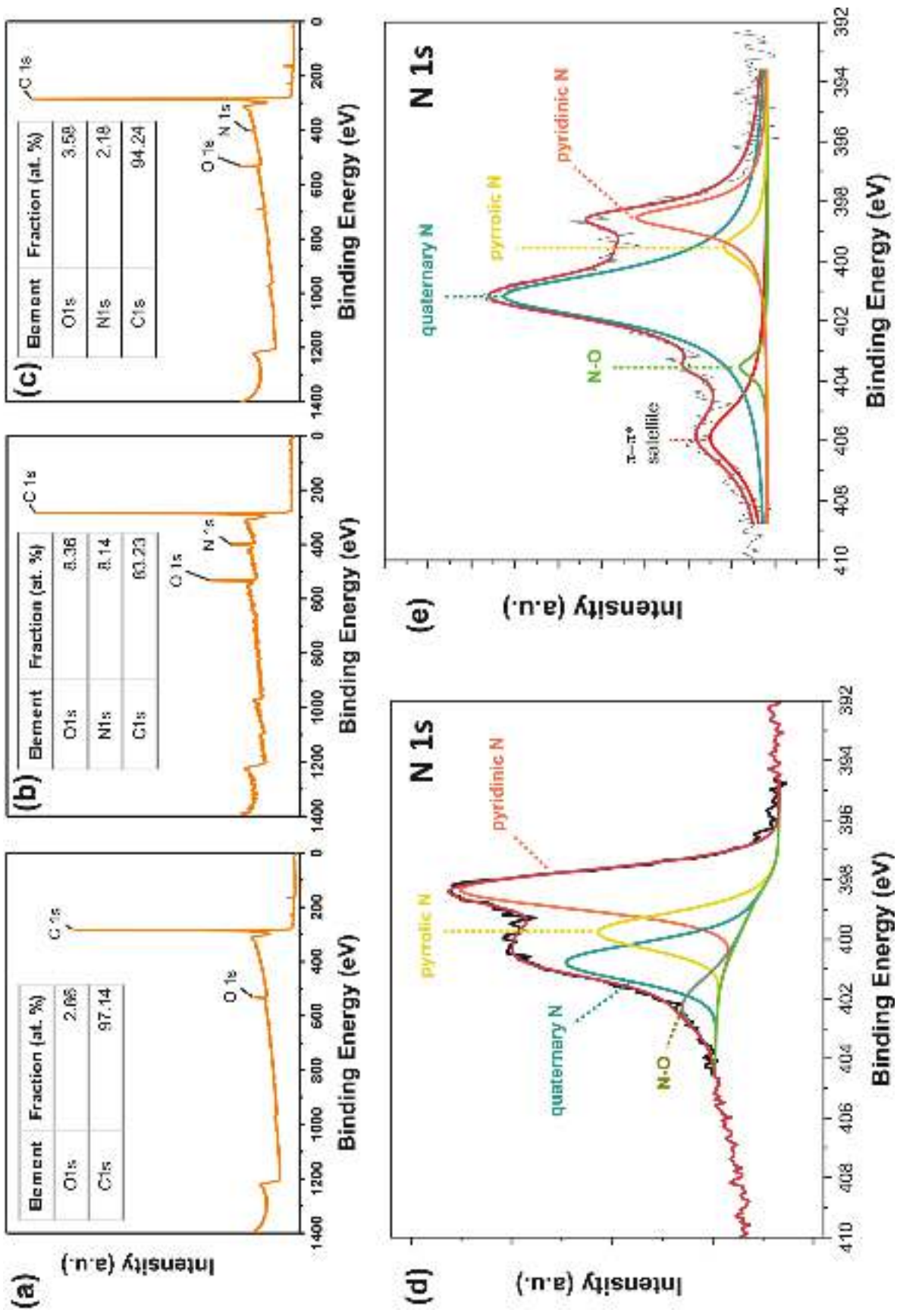

Fig. 2. XPS survey spectra and compositional analyses for (a) CMK-3, (b) N*d*MC-750, and (c) N*d*MC-900. N 1s spectra for (d) N*d*MC-750 and (e) N*d*MC-900 with profiles fitted using three major component peaks representing N atoms at pyridinic, pyrrolic, and quaternary positions.

Table 1
Quantitative analyses of the N structural characteristics of N*d*MC-750, and N*d*MC-900 estimated by fitting the N 1s spectra using three major component peaks corresponding to pyridinic, pyrrolic, and quaternary Ns.

Material/N-type	Quaternary, N_{QN} (%)	Pyrrolic, N_{QL} (%)	Pyridinic, N_{PD} (%)
N*d*MC-750	24.5	20.5	48.2
N*d*MC-900	72.0	7.12	20.3

used to describe the exchange-correlation functional [34]. For the standard computational parameters, a *k*-point mesh was 5 × 5 × 5 with the Monkhorst-Pack scheme and an energy cut-off of at least 500 eV was set for the plane wave basis points. The unit cells and atomic positions were fully relaxed until residual atomic forces were less than 0.01 eV $Å^{-1}$. The DFT-D2 method was also used to consider van der Waals interaction between graphite layers in the form of AB stacking.

3. Results and discussion

3.1. Physicochemical characterization of NdMC

We prepared N*d*MC materials through a previously reported CVD-like process [28,29], where Fe-phthalocyannine (Fe-Pc) served as a carbon and nitrogen source, while SBA-15 served as a rigid but removable silica template during high-temperature pyrolysis and acid leaching, as described in Fig. 1a. Two types of N*d*MC with vastly different degrees of graphitization and nitrogen contents and possessing different surface moieties were prepared at two distinct synthetic temperatures: 750 °C and 900 °C, which are denoted as N*d*MC-750 and N*d*MC-900, respectively. Fig. 1b shows the X-ray diffraction (XRD) patterns of the two materials compared against conventional mesoporous carbon material without nitrogen substitution (CMK-3), manufactured by sucrose nano-casting [35]. The presence of a distinct peak at *ca.* 26° for N*d*MC-900 indicates that it retained a graphitic wall, which was further confirmed by the high intensity ratio, I_G/I_D (0.72), in the corresponding Raman spectra (Fig. 1c). The interlayer distance of the (002) planes and the coherent length (L_c) through the [001] direction for N*d*MC-900 was estimated to be 3.46 Å and 29.0 Å, respectively, in accordance with the nanoscale dimensions of the graphitic wall. This unique networked wall structure of N*d*MC-900 may endow the redox reaction sites with appropriate electrical wiring, that would in turn enhance the electrochemical activity of the cathode. N*d*MC-750 and CMK-3 carbons exhibited broad amorphous peaks (at *ca.* 25° and 22°, respectively) in their XRD patterns and much lower I_G/I_D ratios in their Raman spectra (0.48 and 0.38, respectively), indicating that sp^3–hybridized carbons were dominant in these materials [36,37].

The XPS of N*d*MCs and CMK-3 (Fig. 2a) indicated that the nitrogen

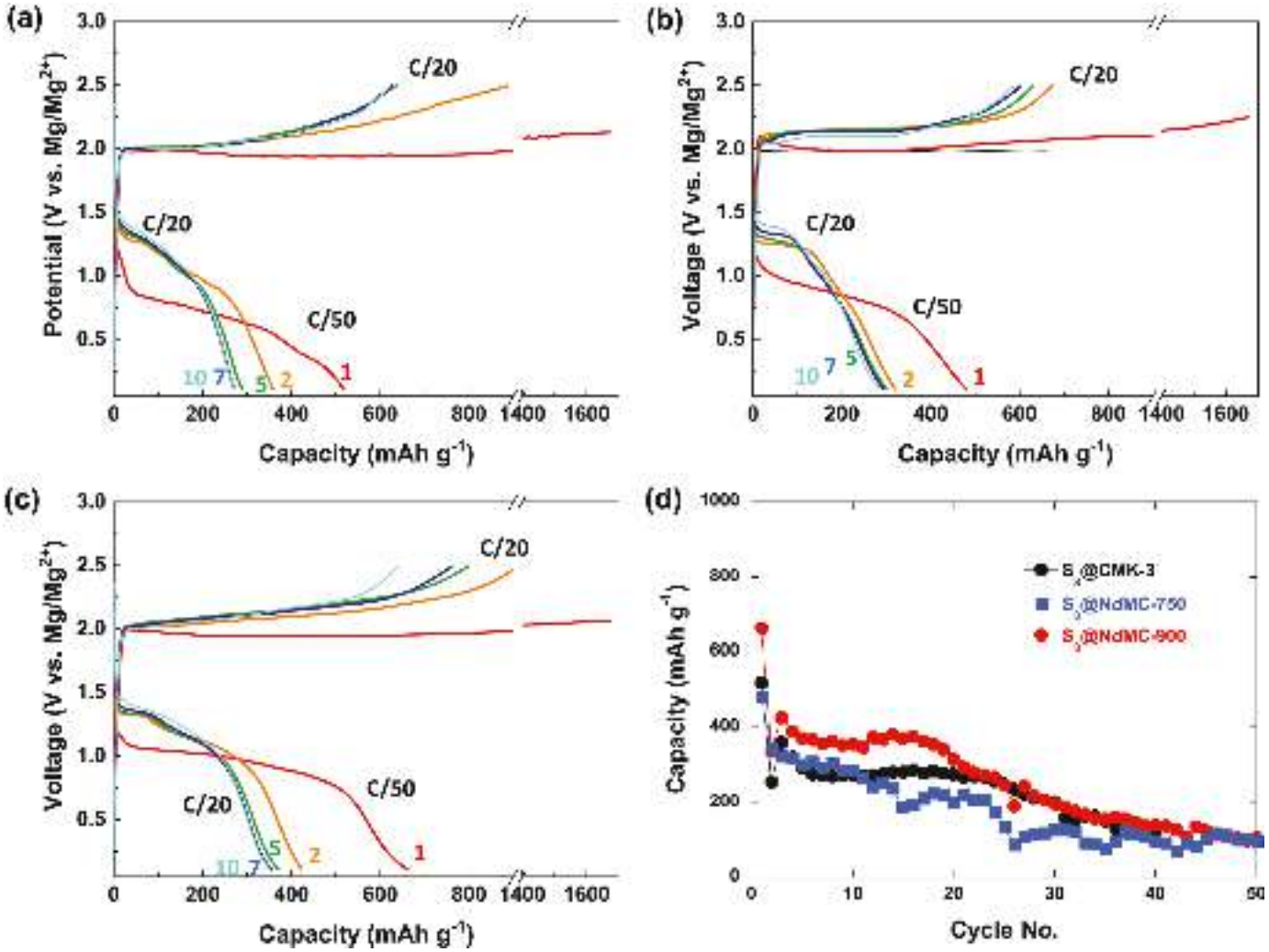

Fig. 3. The discharge-charge profiles of Mg–S batteries with a composite cathode made of (a) S_8@CMK-3, (b) S_8@N*d*MC-750, (c) S_8@N*d*MC-900 in BCM electrolyte, and (d) their cycling capacity retentions. The current density for the first discharge was set to C/50, which was thereafter increased to C/20. 1C-rate corresponds to 1,675 mA g^{-1} of sulfur.

content in N*d*MC-900 was substantially smaller than that of N*d*MC-750 (2.2% vs. 8.1%), implying that the amount and moiety setup of nitrogen in N*d*MC might be tunable by adjusting the pyrolysis temperature [38–40]. The characteristics of nitrogen atoms doped on the carbons were further investigated by fitting the N 1s XPS profiles of N*d*MCs with the major component peaks (Fig. 2d and e), of pyridinic, pyrrolic, and quaternary nitrogen atoms (denoted as N_{PD}, N_{PL}, N_{QN} respectively) as described in Fig. 1a. For N*d*MC-750, the contribution of pyridinic N was the highest (48.2%, 20.5%, and 24.5% for N_{PD}, N_{PL}, and N_{QN}, respectively), whereas for N*d*MC-900, the quaternary N was the major contributor (20.3%, 7.1%, and 72.0% for N_{PD}, N_{PL}, and N_{QD}, respectively). This is further summarized in Table 1. The XRD and Raman analyses indicate that N*d*MC-900 consists of well-developed graphitic walls. Notably, pyridinic N still accounts for approximately 20% of all doped N atoms in N*d*MC-900. We estimated the actual amount of nitrogen contents in N*d*MC carbons and found that *ca.* 80% of quaternary N formed at 750 °C was still preserved at 900 °C, which indicates that N atoms in quaternary positions are relatively more stable at high temperatures than N atoms in other positions. The types and composition of these surface moieties may critically influence the kinetics of Mg–S batteries, as some types of nitrogen-doped sites in carbonaceous materials are known to serve as good anchoring sites for soluble LiPS. This is because of the strong electrostatic attraction between terminal Li ions in LiPS and residual electron pairs in N-dopants in the carbon hosts [23–27].

3.2. Electrochemical performance of Mg batteries using S_8@NdMC composite cathodes

To investigate whether different chemical and structural characteristics of the carbons could influence the electrochemical activity, we evaluated the performance of Mg–S batteries with composite electrodes made of the N*d*MC carbons imbibed with the same relative amount of sulfur (denoted as S_8@N*d*MC-900, S_8@ N*d*MC-750, S_8@CMK-3, respectively). The actual amount of sulfur in the composite was also estimated by TGA (Fig. S1), showing that sulfur constituted *ca.* 50 wt% of the composite as expected. The typical sulfur loading was ~0.7 mg cm^{-2} and the results are shown in Fig. 3a–d. Considering the lethargic cathode kinetics [1–3], a slow current rate of C/50 was applied for the first discharge process, which was thereafter increased to C/20. Among them, S_8@N*d*MC-900 exhibited the highest first-discharge capacity (660 mAh g^{-1}), which was almost 30% greater than the other two composites (~500 mAh g^{-1}). Particularly, the plateau potentials for S_8@N*d*MCs were observed to be 0.2 V or higher than that for S_8@CMK-3 for the first cycle, indicating that N-doping in the carbon materials helps to catalyze the electrochemical reduction of sulfur. At an increased current rate of C/20 applied after the first discharge, S_8@N*d*MC-900 maintained the highest capacity of *ca.* 400 mAh g^{-1} up to 20 cycles, whereas the other two composite electrodes exhibited only 300 mAh g^{-1}. A similar tendency was still observed at an even higher current rate of C/10; S_8@N*d*MC-900 still exhibited 40% higher discharge-capacity than others, and the electrodes with N-doped carbons (S_8@N*d*MCs) exhibited discharge potentials of 0.2 V or higher during the first cycle (Fig. S2). The capacity fading commonly observed for all carbon composites after 20 cycles is probably due to the impedance buildup on the Mg metal surface, and the loss of active materials on the cathode as solubilized sulfur or MgPS might diffuse to the anode side, reacting with Mg metal to form ion-insulating precipitates on the surface [5,12,41]. The precipitation of solubilized MgPS or its decomposition products on the Mg anode was confirmed by observing the surface of the cycled anodes. Fig. S3 exhibited that smooth, rounded particles with sulfur-rich composition was deposited on the Mg surface even after the completion of the very first cycle, strongly implying that polysulfide intermediates might be quite soluble in the electrolyte, and the low coulombic efficiency observed in Mg–S cells (Fig. S4) was primarily ascribed to the polysulfide shuttle effect.

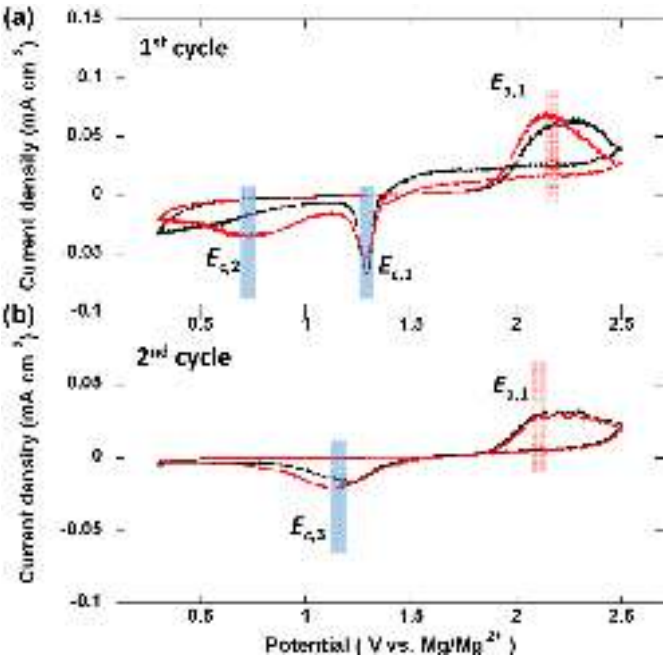

Fig. 4. Cyclic voltammograms of (a) the first cycle and (b) the second cycle for the electrode made of S_8@CMK-3 (black), and S_8@N*d*MC-900 (red) in BCM, where various cathodic peaks ($E_{c,1}$, $E_{c,2}$, $E_{c,3}$), and anodic peaks ($E_{a,1}$) are shown. The scan rate was 0.02 mV s^{-1}. (For interpretation of the references to colour in this figure legend, the reader is referred to the Web version of this article.)

Fig. 4 shows the cyclic voltammograms (CVs) of the two composite electrodes (S_8@N*d*MC-900 and S_8@CMK-3) obtained at a scan rate of 0.02 mV s^{-1}. The first cathodic scan exhibited two distinct peaks, where the sharp first peak ($E_{c,1}$) likely represents the transformation of S_8 to long-chain polysulfides like MgS_8, whereas the broad second peak ($E_{c,2}$) could result from the dissociation of MgS_8 into MgS. To verify this hypothesis, we prepared Mg polysulfide chemically using a previously reported procedure [31]. Specifically, we prepared Mg(1-methylimidzole)$_6$]S_8 (denoted as $MgIm_6S_8$) by reacting S_8 and Mg metal powder in 1-methylimidzaole and carried out a linear sweep voltammetric measurement (LSV) of $MgIm_6S_8$ (3.2 mM) with BCM as an electrolyte and N*d*MC-900 without sulfur imbibition as the working electrode (Fig. S5). The open circuit potential (OCP) was found to be around 0.8 V, which was quite different from the composite cathodes with S_8 loading (*ca.* 1.4 V). Moreover, a distinct reduction peak at 0.75 V ($E_{c,4}$) had appeared, which could be attributed to $E_{c,2}$ of S_8@N*d*MC-900. Therefore, it is reasonable to assume that $E_{c,1}$ corresponds to the transformation of S_8 to MgS_8, while $E_{c,2}$ accounts for the further dissociation of MgS_8 into MgS. Notably, the $E_{c,2}$ peaks for S_8@N*d*MC-900 were well-defined, as opposed to S_8@CMK-3, which did not show any distinct peaks for $E_{c,2}$. This implies that N-doped carbon can enhance the reaction kinetics associated with $E_{c,2}$. After the first cycle, the cathodic scan showed only a single peak ($E_{c,3}$), which indicates changes in the reaction mechanism (Fig. 4b). This implies that the Mg polysulfide formation and disproportionation into the final product occurred simultaneously during the second cycle.

3.3. UV–Visible studies on reaction mechanism

To further study the effectiveness of N*d*MC for enhancing the fragmentation of Mg polylsulfides, we allowed the Mg polysulfide species, which were fixed onto the surface of the carbon materials, to decompose chemically to shorter chains and then estimated the amount of Mg polysulfide species present in the electrolyte. To that effect, a set amount of carbon material (N*d*MC-900, CMK-3) was added to an electrolyte

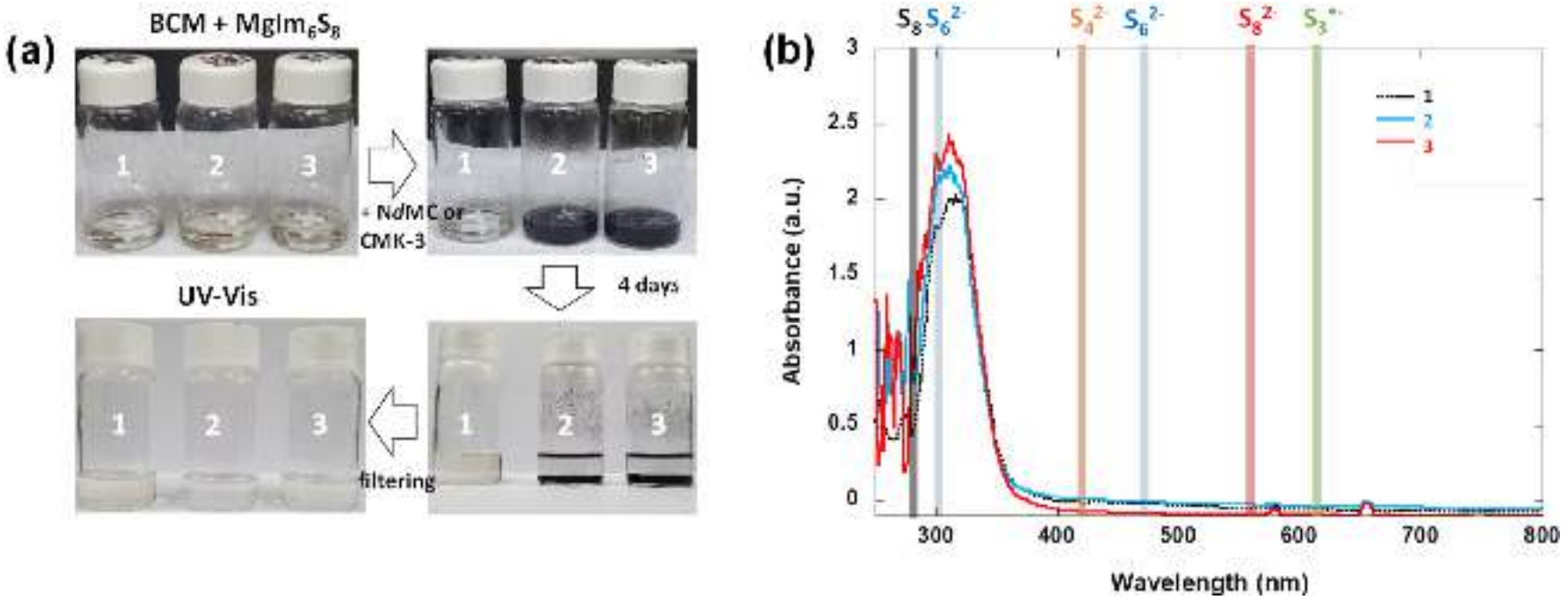

Fig. 5. UV–Vis studies on the interactions between $MgIm_6S_8$ and carbon materials; (a) Process of preparation of the solutions. The solution prepared without any carbon addition to the electrolyte is labelled as 1, the one with N*d*CM-900 addition as 2, and the one with CMK-3 addition as 3. (b) UV–Vis spectra for all the solutions. All solutions initially contain the same amount of $MgIm_6S_8$ (3.2 mM).

Table 2
Elemental analyses of the solutions prepared from $MgIm_6S_8$ in BCM electrolyte without any carbon addition (solution #1), the one with N*d*MC-900 addition (solution #2), and the one with CMK-3 addition (solution #3). For detailed preparation, see the experimental section.

Element	S (mol/L)	Mg (mol/L)
solution #1	0.074	0.0048
solution #2	0.069	0.0037
solution #3	0.037	0.0033

solution containing $MgIm_6S_8$ (*ca.* 3.2 mM) and was stirred for four days before analysis (Fig. 5a). Interestingly, we observed that $MgIm_6S_8$ readily dissolved in the BCM electrolyte to form a transparent solution, as opposed to dimethoxyethane (DME), in which it was hardly soluble [13,14]. This suggests that the relatively electron-rich $MgIm_6S_8$ might be further coordinated with the strong electron acceptor THFPB, resulting in a multi-complex species that is highly soluble in the BCM electrolyte. The amount of sulfur-bearing species dissolved in each electrolyte after four days of stirring was analyzed using ICP-OES, and the results are tabulated in Table 2. The results reveal that while the sulfur content in the electrolyte decreased sharply by half for N*d*MC-900, it was diminished by only ~7% for CMK-3. This indicates that N*d*MC-900 absorbed $MgIm_6S_8$ more readily and catalyzed its dissociation more efficiently than CMK-3. UV–Visible spectroscopy was employed to characterize the polysulfide species present in the electrolyte (Fig. 5b). The spectra of $MgIm_6S_8$/BCM, both before and after the addition of carbon materials, exhibit a sharp absorption peak at 320 nm, which could be assigned to S_6^{2-} [13,14,17]. This indicates that S_8^{2-} might disproportionate into S_6^{2-} and S_8 in the BCM electrolyte (*i.e.*, $S_8^{2-} \rightarrow S_6^{2-} + (1/4)S_8$). In Fig. S6, the absorption peak of $MgIm_6S_8$/BCM is compared with that of elemental sulfur (S_8) dissolved in the electrolyte, which might be produced as a result of the disproportionation of $MgIm_6S_8$ and S_6^{2-}. For S_8/BCM, a wide and intense absorption ranging from 250 to 300 nm was observed, which may overlap in part with that of S_6^{2-}. Because a sizable absorption intensity from 250 to 300 nm was observed for all $MgIm_6S_8$/BCM specimens, some dissolved S_8 was likely present in all those cases. These results imply that N*d*MC-900 effectively adsorbed and catalyzed the dissociation of S_6^{2-}.

3.4. Density functional theory calculation

To gain more insight into the catalytic effect of N moieties on MgPS dissociation, we modelled the Mg adsorption behavior in the N-doped carbons for three main bonding configurations, *i.e.*, nitrogen atoms in pyridinic, pyrrolic, and quaternary positions. Since the strong adsorption of LiPS on N-doped carbons has been well documented [23–27], we focused on the effect of different cations, *i.e.*, Mg^{2+} on this phenomenon. The most favorable Mg adsorption site was determined by considering three possible adsorption sites on the graphitized plane: at the center of the hexagonal ring, on the top of the C or N atom, and on the bridge site above the midpoint of the C–C or C–N bond, as shown in Fig. 6a. DFT calculations were carried out to determine the most stable configurations of a Mg interstitial atom in various N-doping configurations, and the calculated values of the Mg interstitial formation energy are shown in Figs. S7 and 6b. A more negative value of the Mg interstitial formation energy indicates a stronger interaction between the N-doped carbon structure and Mg atoms. We found that the pyridinic N exhibited a significantly higher adsorption energy of −0.1182 eV towards Mg than the pyrrolic (−0.0283 eV) and quaternary (1.7285 eV) Ns. These results are similar to what has been observed in the interactions between N-doped carbon and LiPS [25,26]. We observed that the N atoms at quaternary positions did not form favorable bonds with Mg atoms. This suggests that the pyridinic N would be the most efficient at enhancing the adsorption of Mg polysulfides, and thus would lead to the best catalytic effect for polysulfide dissociation. Meanwhile, electron accessibility to the redox sites is another crucial factor that affects the kinetics of redox reactions. Electrical conductivity in carbon materials can be achieved via a graphitic structure with doped nitrogen atoms, constituted by quaternary Ns. Therefore, the remarkable electrochemical performance of S_8@N*d*MC-900 is likely due to the N atoms being well-deployed in the pyridinic and quaternary positions across the N*d*MC-900 material.

3.5. Discussion

Based on the observations, we deduced that the reaction mechanism of the Mg–S battery cathode in the BCM electrolyte with N*d*MC hosts likely involves two major reaction steps. In the first step, S_8 molecules are electrochemically reduced to S_8^{2-} (*e.g.*, $S_8 + Mg^{2+} + 2e^- \rightarrow MgS_8$), which is then dismutated to S_6^{2-} and S_8 (*e.g.*, $S_8^{2-} \rightarrow S_6^{2-} + (1/4)S_8$). The S_6^{2-} species are readily soluble in the electrolyte but are strongly adsorbed on N-doped sites, particularly at the pyridinic positions. In the second step, S_6^{2-} is likely electrochemically dissociated into MgS (*i.e.*, $S_6^{2-} + 6Mg^{2+} + 12e^- \rightarrow 6MgS$). This step may involve multiple reaction steps, including the adsorption of $S_6^{2-}$and its dissociation into shorter-chain polysulfides, followed by further dismutations. N*d*MC materials can accelerate the slow second step of the reaction on N-doped sites since the pyridinic and pyrrolic Ns may act as catalytic sites for

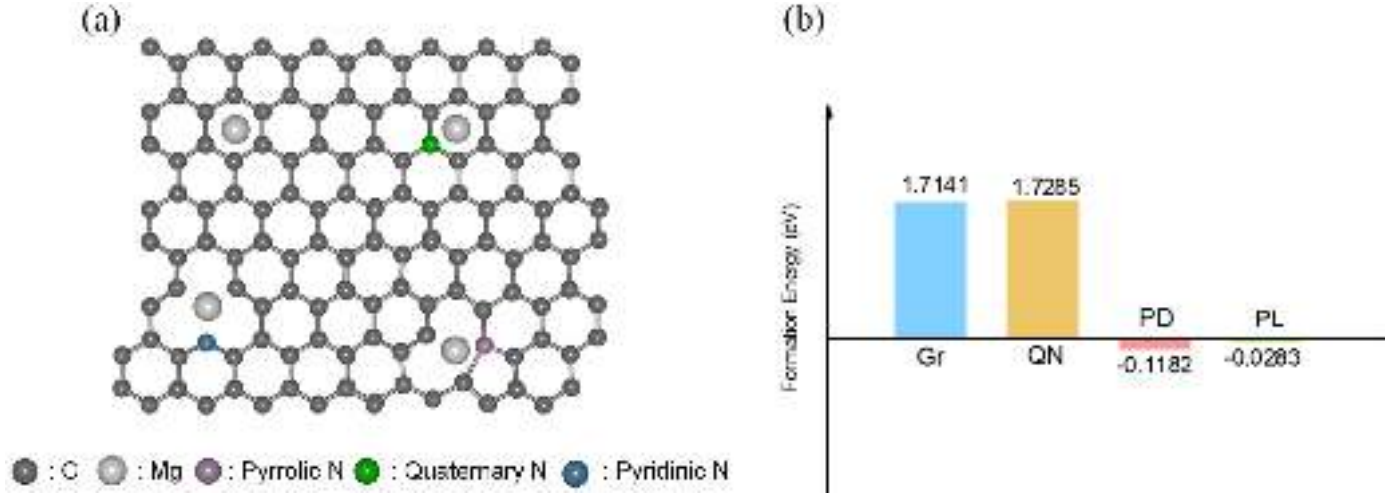

Fig. 6. (a) Mg adsorption configuration on the graphitized plane: pristine, quaternary-N, pyridinic-N, and pyrrolic-N doped cases. (b) Adsorption formation energy of Mg on the N-doped graphitized plane.

polysulfide adsorption/fragmentation. The superior performance of S_8@N*d*MC-900 compared to S_8@N*d*MC-750 was probably because of the synergetic effect of these catalytic reactions aided by functional surface catalytic sites, and the higher electron accessibility of N*d*MC-900 to the redox sites due to its graphitic wall structure. In the meantime, it is also obvious that N*d*MC alone cannot control the shuttle phenomenon by the soluble MgPS intermediates completely, judging from the poor coulombic efficiency of the battery cells. This aspect is under investigation as our next topic and will be reported in our future communications.

4. Conclusions

In this work, we demonstrate that N-doped mesoporous graphitic carbon materials with tuned nitrogen functionalities can be utilized as catalytic hosts for enhancing polysulfide fragmentation and electron access to the redox active sites in Mg–S batteries. In N*d*MC-900, the surface nitrogen atoms at the pyridinic and pyrrolic positions can enhance the kinetics of the electrochemical reduction of S_6^{2-} to MgS. Moreover, the graphitic wall structure promotes electron transport to the reaction sites. This synergistic effect enables S_8@N*d*MC-900 to exhibit significantly superior reversible capacity and good capacity retention in Mg–S batteries.

CRediT authorship contribution statement

Minseok Lee: Investigation, Methodology, Data curation, Visualization, Software. **Minji Jeong:** Investigation, Data curation, Software. **Youn Shin Nam:** Formal analysis. **Janghyuk Moon:** Formal analysis. **Minah Lee:** Investigation, Formal analysis. **Hee-Dae Lim:** Formal analysis. **Dongjin Byun:** Formal analysis. **Taeeun Yim:** Formal analysis. **Si Hyoung Oh:** Conceptualization, Supervision, Writing – review & editing.

Declaration of competing interest

The authors declare that they have no known competing financial interests or personal relationships that could have appeared to influence the work reported in this paper.

Acknowledgments

This work was financially supported by the Korea Institute of Science and Technology (KIST) institutional program (project No. 2E31862), the National Research Foundation of Korea (NRF) (NRF-2021R1A2C2008680, NRF-2021R1C1C1008383).

Appendix A. Supplementary data

Supplementary data to this article can be found online at https://doi.org/10.1016/j.jpowsour.2022.231471.

References

[1] Z. Zhang, S. Dong, Z. Cui, A. Du, G. Li, G. Cui, Small Methods 2 (2018), 1800020.
[2] Z. Zhao-Karger, M. Fichtner, MRS Communications 7 (2017) 770–784.
[3] L. Kong, C. Yan, J.-Q. Huang, M.-Q. Zhao, M.-M. Titirici, R. Xiang, Q. Zhang, Energy Environ. Mater. 1 (2018) 100–112.
[4] Z. Zhao-Karger, X. Zhao, D. Wang, T. Diemant, R.J. Behm, M. Fichtner, Adv. Energy Mater. 5 (2015), 1401155.
[5] Z. Zhao-Karger, R. Liu, W. Dai, Z. Li, T. Diemant, B.P. Vinayan, C.B. Minella, X. Yu, A. Manthiram, R.J. Behm, M. Ruben, M. Fichtner, ACS Energy Lett. 3 (2018) 2005–2013.
[6] B.P. Vinayan, Z. Zhao-Karger, T. Diemant, V.S.K. Chakravadhanula, N. I. Schwarzburger, M.A. Cambaz, R.J. Behm, C. Kűbel, M. Fichtner, Nanoscale 8 (2016) 3296–3306.
[7] Z. Zhang, Z. Cui, L. Qiao, J. Guan, H. Xu, X. Wang, P. Hu, H. Du, S. Li, X. Zhou, S. Dong, Z. Liu, G. Cui, L. Chen, Adv. Energy Mater. 7 (2017), 1602055.
[8] A. Du, Z. Zhang, H. Qu, Z. Cui, L. Aiao, L. Wang, J. Chai, T. Lu, S. Dong, T. Dong, H. Xu, X. Zhou, G. Cui, Energy Environ. Sci. 10 (2017) 2616–2625.
[9] H. Xu, Z. Zhang, Z. Cui, A. Du, C. Lu, S. Dong, J. Ma, X. Zhou, G. Cui, Electr. Commun. 83 (2017) 72–76.
[10] A. Robba, A. Vizintin, J. Bitenc, G. Mali, I. Arčon, M. Kavčič, M. Žitnik, K. Bučar, G. Aquilanti, C. Martineau-Corcos, A. Randon-Vitanova, R. Dominko, Chem. Mater. 29 (2017) 9555–9564.
[11] T. Gao, S. Hou, F. Wang, Z. Ma, X. Li, K. Xu, C. Wang, Angew. Chem. Int. Ed. 56 (2017) 13526–13530.
[12] H.O. Ford, E.S. Doyle, P. He, W.C. Boggess, A.G. Oliver, T. Wu, G.E. Sterbinsky, J. L. Schaefer, Energy Environ. Sci. 14 (2021) 890–899.
[13] G. Bieker, J. Wellmann, M. Kolek, K. Jalkanen, M. Winter, P. Bieker, Phys. Chem. Chem. Phys. 19 (2017) 11152–11162.
[14] G. Bieker, D. Diddens, M. Kolek, O. Borodin, M. Winter, P. Bieker, K. Jalkanen, J. Phys. Chem. C 122 (2018) 21770–21783.
[15] T. Gao, X. Ji, S. Hou, X. Fan, X. Li, C. Yang, F. Han, F. Wang, J. Jiang, K. Xu, C. Wang, Adv. Mater. 30 (2018), 1704313.
[16] Y.-C. Lu, Q. He, H.A. Gasteiger, J. Phys. Chem. C 118 (2014) 5733–5741.
[17] C. Barchasz, F. Molton, C. Duboc, J.-C. Laprêtre, S. Patoux, F. Alloin, Anal. Chem. 84 (2012) 3973–3980.
[18] M. Cuisinier, P.-E. Cabelguen, S. Evers, G. He, M. Kolbeck, A. Garsuch, T. Bolin, M. Balasubramanian, L.F. Nazar, J. Phys. Chem. Lett. 4 (2013) 3227–3232.
[19] X. Liang, C. Hart, Q. Pang, A. Garsuch, T. Weiss, L.F. Nazar, Nat. Commun. 6 (2015) 5682, https://doi.org/10.1038/ncomms6682.
[20] T.-G. Jeong, D.S. Choi, H. Song, J. Choi, S.A. Park, S.H. Oh, H. Kim, Y. Jung, Y.-T. Kim, ACS Energy Lett. 2 (2017) 327–333.
[21] N. Mosavati, V.R. Chitturi, S.O. Salley, K.Y.S. Ng, J. Power Sources 321 (2016) 87–93.
[22] J. Choi, T.-G. Jeong, B.W. Cho, Y. Jung, S.H. Oh, Y.-T. Kim, J. Phys. Chem. C 122 (2018) 7664–7669.
[23] J. Song, T. Xu, M.L. Gordin, P. Zhu, D. Lv, Y.-B. Jiang, Y. Chen, Y. Duan, D. Wang, Adv. Funct. Mater. 24 (2014) 1243–1250.
[24] J. Song, M.L. Gordin, T. Xu, S. Chen, Z. Yu, H. Sohn, J. Lu, Y. Ren, Y. Duan, D. Wang, Angew. Chem. 127 (2015) 4399–4403.
[25] T.-Z. Hou, H.-J. Peng, J.-Q. Huang, Q. Zhang, B. Li, 2D Mater. 2 (2015), 014011.
[26] L.-C. Yin, J. Liang, G.-M. Zhou, F. Li, R. Saito, H.-M. Cheng, Nano Energy 25 (2016) 203–210.
[27] S. Dörfler, P. Strubel, T. Jaumann, E. Troschke, F. Hippauf, C. Kensy, A. Schökel, H. Althues, L. Giebeler, S. Oswald, S. Kaskel, Nano Energy 54 (2018) 116–128.
[28] K.T. Lee, X. Ji, M. Rault, L.F. Nazar, Angew. Chem. 121 (2009) 5771–5775.
[29] E.S. Shin, M.-S. Kim, W.I. Cho, S.H. Oh, Nanoscale Res. Lett. 8 (2013) 343.
[30] D. Zhao, J. Feng, Q. Huo, N. Melosh, G.H. Fredrickson, B.F. Chmelka, G.D. Stucky, Science 279 (1998) 548–552.
[31] S. Dev, E. Ramli, T.B. Rauchfuss, S.R. Wilson, Inorg. Chem. 30 (1991), 2541-2519.
[32] P.E. Blöchl, Phys. Rev. B 50 (1994) 17953–17979.
[33] G. Kresse, J. Hafner, Phys. Rev. B 48 (1993) 13115–13118.
[34] J.P. Perdew, K. Burke, M. Ernzerhof, Phys. Rev. Lett. 77 (1996) 3865–3868.
[35] S. Jun, S.H. Joo, R. Ryoo, M. Kruk, M. Jaroniec, Z. Liu, T. Ohsuna, O. Terasaki, J. Am. Chem. Soc. 122 (2000) 10712–10713.
[36] A.C. Ferrari, J. Robertson, Phys. Rev. B 61 (2000) 14095–14107.
[37] A.C. Ferrari, D.M. Basko, Nat. Nanotechnol. 8 (2013) 235–246.
[38] L. Zhao, X.-L. Sui, Q.-Y. Zhou, J.-Z. Li, J.-J. Zhang, G.-S. Huang, Z.B. Wang, J. Mater. Chem. A 6 (2018) 6212–6219.
[39] Q. Zhou, J. Cai, Z. Zhang, R. Gao, B. Chen, G. Wen, L. Zhao, Y. Deng, H. Dou, X. Gong, Y. Zhang, Y. Hu, A. Yu, X. Sui, Z. Wang, Z. Chen, Small Methods 5 (2021), 2100024.
[40] C. Maddi, F. Bourquard, V. Barnier, J. Avila, M.-C. Asensio, T. Tite, C. Donnet, F. Garrelie, Sci. Rep. 8 (2018) 3247.
[41] B.P. Vinayan, H. Euchner, Z. Zhao-Karger, M.A. Cambaz, Z. Li, T. Diemant, R. J. Behm, A. Gross, M. Fichtner, J. Mater. Chem. A 7 (2019) 25490–25502.